



## Article

# Synthesis and Characterization of Lithium Phosphate ( $\text{Li}_3\text{PO}_4$ ) as a Solid Electrolyte

Seybou Yacouba Zakariyaou Hua Ye \* and Chongwen Jiang

Department of Chemical Engineering and Technology, School of Chemistry and Chemical Engineering, Central South University, Changsha 410083, China; 212318002@csu.edu.cn (S.Y.Z.); jcwcsu@csu.edu.cn (C.J.)

\* Correspondence: yehua308@csu.edu.cn

**Abstract:** Due to its high thermal stability, environmental friendliness, and safety, lithium phosphate ( $\text{Li}_3\text{PO}_4$ ) is used as a solid electrolyte in battery applications, but it is usually used with dopants due to its lower ionic conductivity, which is required for ion transport. However, due to its stability and environmentally friendly aspect, lithium phosphate is still a hot topic among suitable energy materials that need further research to improve its electrochemical properties. In the current work, a novel synthesis of lithium phosphate was proposed from the raw materials lithium carbonate ( $\text{Li}_2\text{CO}_3$ ) and trisodium phosphate dodecahydrate ( $\text{Na}_3\text{PO}_4 \cdot 12\text{H}_2\text{O}$ ) under suitable stoichiometric conditions using the co-precipitation method. In the set of synthesized samples, a single-phase  $\beta$ - $\text{Li}_3\text{PO}_4$  (named LPO-4) with 99.7% purity and 93.49% yield was successfully prepared under appropriate stoichiometric conditions and pH 13 at 90 °C. The average particle size was 10 nm with a large surface area of  $9.02 \text{ m}^2\text{g}^{-1}$ . Electrochemical impedance spectroscopy (EIS) of LPO-4 revealed a conductivity of  $7.1 \times 10^{-6} \text{ S.cm}^{-1}$  at room temperature and  $2.7 \times 10^{-5} \text{ S.cm}^{-1}$  at 80 °C with a low activation energy of 0.38 eV. This performance is attributed to the morphology of the nanotubes and the smaller particle size, which enlarge the reaction interfaces and shorten the diffusion distance of lithium ions. The kinetic and thermodynamic key parameters showed that the  $\beta$ - $\text{Li}_3\text{PO}_4$  exhibits thermal stability in the room temperature range up to 208.8 °C. All these property values indicate a promising application of lithium phosphate as a solid electrolyte in solid-state batteries and a new route for further investigation.



**Citation:** Zakariyaou, S.Y.; Ye, H.; Jiang, C. Synthesis and Characterization of Lithium Phosphate ( $\text{Li}_3\text{PO}_4$ ) as a Solid Electrolyte. *Batteries* **2024**, *10*, 429. <https://doi.org/10.3390/batteries10120429>

Academic Editors: Shaokun Chong and Diana Golodnitsky

Received: 13 October 2024

Revised: 26 November 2024

Accepted: 30 November 2024

Published: 3 December 2024



**Copyright:** © 2024 by the authors. Licensee MDPI, Basel, Switzerland. This article is an open access article distributed under the terms and conditions of the Creative Commons Attribution (CC BY) license (<https://creativecommons.org/licenses/by/4.0/>).

## Highlights

1. The single-phase and high-purity  $\beta$ - $\text{Li}_3\text{PO}_4$  was synthesized by a facile co-precipitation method.
2. A particle nanoscale sample with a high surface area was successfully prepared.
3. A solid electrolyte, lithium phosphate, with high ionic conductivity was achieved.
4. Kinetic and thermodynamic studies established lithium phosphate behavior as a function of the temperature.

## 1. Introduction

Lithium element has become an essential component of the new generation of sustainable and green energy technologies. Lithium phosphate produced from lithium plays a crucial role in modern battery technology and biomass conversion as a catalyst [1] due to its excellent electrochemical and catalytic performance in alkylene oxide isomerization reactions. In lithium-ion batteries, it is usually used as a solid electrolyte or as a protective coating rather than directly as a cathode material [2,3]. Due to the safety issues associated with liquid electrolytes, such as leakage, explosion, and fire risks, a solid electrolyte has

been developed as an alternative solution to overcome these problems and improve the energy density of lithium-ion batteries [4,5].

Therefore, researchers have applied various techniques to improve conductivity, including particle size modulation and doping with some elements (iron, cobalt, and nickel) [6], using different synthesis methods, including the plasma spray [2,7], the co-precipitation [8], the pulsed laser decomposition [9], wet chemical (conductivity of  $4.65 \times 10^{-8} \text{ S.cm}^{-1}$ ) [10] and the solid-state methods [11]. These approaches for producing lithium phosphate include a co-precipitation method, which is the best way to obtain a homogeneous lithium phosphate product under suitable stoichiometric conditions and pH values due to the high ion exchange. In the co-precipitation method, several routes were explored by a combination of various sources of lithium (hydroxide, carbonate, etc.) and phosphate ions (phosphoric acid, ammonium dihydrogen phosphate, sodium phosphate, etc.), as shown in Table 1.

**Table 1.** Basic conditions for the synthesis of lithium phosphate.

Lithium Source	Phosphate Source	pH Control Reagent	Reaction Temperature °C	Reaction Time/min	pH	Ref.
Li <sub>2</sub> CO <sub>3</sub>	Na <sub>3</sub> PO <sub>4</sub> •10H <sub>2</sub> O	HCl; NaOH	70–78	20–25	12.5–13	[12]
LiOH•H <sub>2</sub> O	NH <sub>4</sub> H <sub>2</sub> PO <sub>4</sub>	-	200	60	-	[13]
LiOH	H <sub>3</sub> PO <sub>4</sub>	-	>80	-	7.5	[14]
Li <sub>2</sub> CO <sub>3</sub>	Na <sub>3</sub> PO <sub>4</sub> •10H <sub>2</sub> O	HCl	>90	60	>12	[15]
Spent battery	H <sub>3</sub> PO <sub>4</sub>	-	70–90	60–120	7–8	[16]

He Guoduan et al. [12] extracted the lithium from the mother liquor of lithium carbonate precipitation to obtain high purity of lithium phosphate in the temperature range of 70–78 °C at a pH of 12.5–13. Norikazu Ishigaki and Junji Akimoto [17] synthesized lithium phosphate as a solid electrolyte for batteries at room temperature and investigated its phase transformation from  $\beta\text{-Li}_3\text{PO}_4$  to  $\gamma\text{-Li}_3\text{PO}_4$  type. The challenge is to propose the most cost-effective high-purity lithium phosphate and improve its ionic conductivity ( $10^{-10} \text{ S.cm}^{-1}$  at room temperature [8]) with excellent electrochemical performance. Some researchers propose to reduce the particle size to the nanoscale due to the increased surface area, which could establish a balance between the ion transport pathways and structural integrity [2].

However, a simple method to prepare Li<sub>3</sub>PO<sub>4</sub> by considering the proper stoichiometry and studying the key kinetic and thermodynamic parameters may be crucial to understanding the properties, behavior, and potential of lithium phosphate (Figure 1).

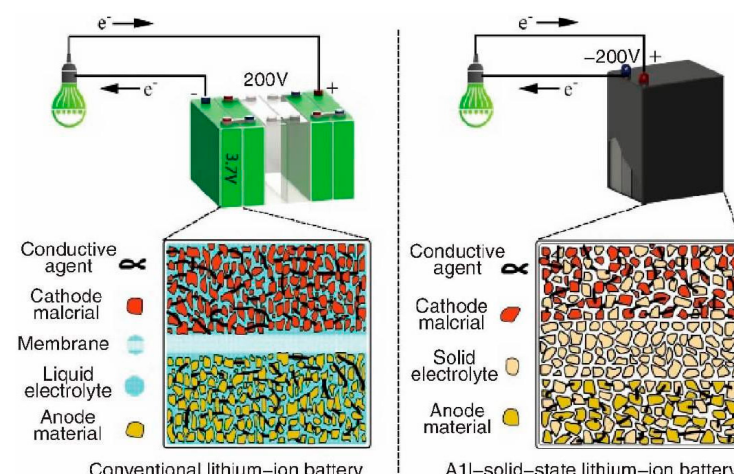


**Figure 1.** A typical solid-state battery: A solid electrolyte, anode material, and conductive agent. Copyright permission obtained from the author [18].

Herein, we proposed a new preparation of lithium phosphate ( $\text{Li}_3\text{PO}_4$ ) as a solid electrolyte from lithium mother liquor ( $\text{Li}_2\text{CO}_3$ ) and the phosphate source trisodium phosphate dodecahydrate ( $\text{Na}_3\text{PO}_4 \cdot 12\text{H}_2\text{O}$ ) for solid-state batteries. To improve the lower conductivity of lithium phosphate, the average particle size was set to a nanoscale of 10 nm with a micropore volume close to zero. This resulted in nanostructured  $\text{Li}_3\text{PO}_4$ , which improves its electrochemical performance by reducing the diffusion pathways for lithium ions. The kinetic and thermodynamic models of Coats and Redfern were developed using the constants of Plank and Boltzmann to determine the sample thermal behavior, including mass loss phases, activation energy ( $E_a$ ), entropy changes ( $\Delta S$ ), enthalpy changes ( $\Delta H$ ), Gibbs free energy changes ( $\Delta G$ ), and pre-exponential factor ( $A$ ).

## 2. Experimental Procedures and Characterization

The raw materials of lithium mother liquor ( $\text{Li}_2\text{CO}_3$ ) and the phosphate source trisodium phosphate dodecahydrate ( $\text{Na}_3\text{PO}_4 \cdot 12\text{H}_2\text{O}$ ) were purchased from the National Pharmaceutical Group Chemical Reagent Co., Ltd. (Shanghai, China).

### 2.1. Titration

The titration procedure (acid mixture): 0.25 g of the lithium carbonate sample was dissolved in 50 mL of deionized solution and stirred well until the solid was completely dissolved. Eight drops of the indicator bromocresol green-methyl red solution (3:1) were added to this solution, which turned green. The titration acid solution was prepared from 50 mL chloric acid (HCl, 0.4996 mol/L) and distilled water (1:1). Using the titrator, the acid solution was first gradually added to the sample solution in the round bottom flask and stirred until the solution turned red. This solution was then heated for 2 min (the color must turn green again) and allowed to cool naturally. The titration was continued the second time; generally, one or two drops of acid were sufficient for the sample solution to turn red. The titration was stopped when the solution turned red, and the acid solution used was measured, as presented in Figure 2. Then, the purity was calculated through the following equation:  $W_{\text{Li}_2\text{CO}_3} = \frac{C_B \cdot V \cdot M}{m^2 \cdot 1000} \cdot 100$ .  $C_B$ : HCl concentration in the solution (1:1) ( $C_B = 0.2498 \text{ mol/L}$ );  $V$ : measured volume (mL) of HCl injected in the tested solution during titration;  $M$ :  $\frac{1}{2}$  of the mass molar (g/mol) of lithium  $\text{Li}_2\text{CO}_3$ ;  $m$ : mass (g) of  $\text{Li}_2\text{CO}_3$  tested sample. For example:  $W_{\text{Li}_2\text{CO}_3} = \frac{0.2498 \text{ mol/L} \cdot 28.80 \text{ mL} \cdot 36.94 \text{ g/mol}}{0.2720 \text{ g} \cdot 1000} \cdot 100 = 97.704\%$ .

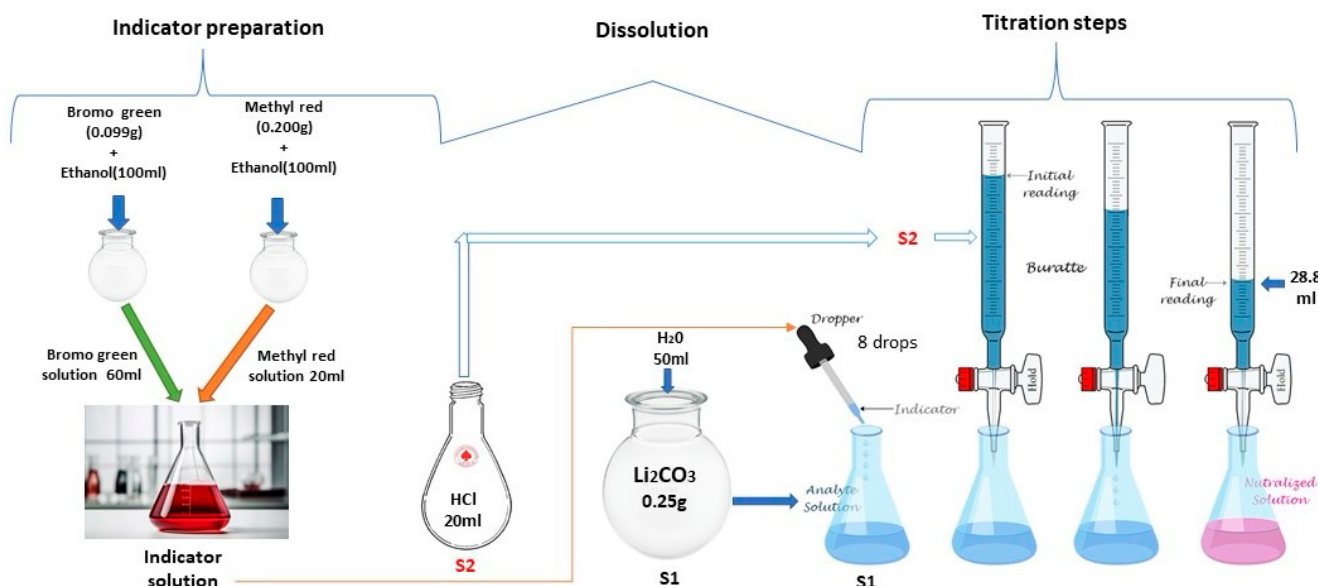


**Figure 2.** Titration steps for lithium carbonate purity testing.

## 2.2. Preparation

Figure 3 describes the Lithium phosphate preparation procedure and the main steps for removal of impurities. The  $\text{Li}_3\text{PO}_4$  samples were prepared using co-precipitation. First, 3 g of lithium carbonate ( $\text{Li}_2\text{CO}_3$ ) sample was dissolved in deionized water at room temperature to obtain a lithium concentration of 0.21 mol/L ( $\text{Li}^+$ ) in the solution. The initial pH of the sample solution was adjusted to 5–5.5 by adding chloric acid (HCl, 36–38%). After stirring at 70 °C for 20–25 min to remove the carbonate ions in the solution, the pH was readjusted to 12–13 by adding NaOH (1%) and 0.025–0.5 g·L<sup>-1</sup> and EDTA (ethylenediaminetetraacetic acid).

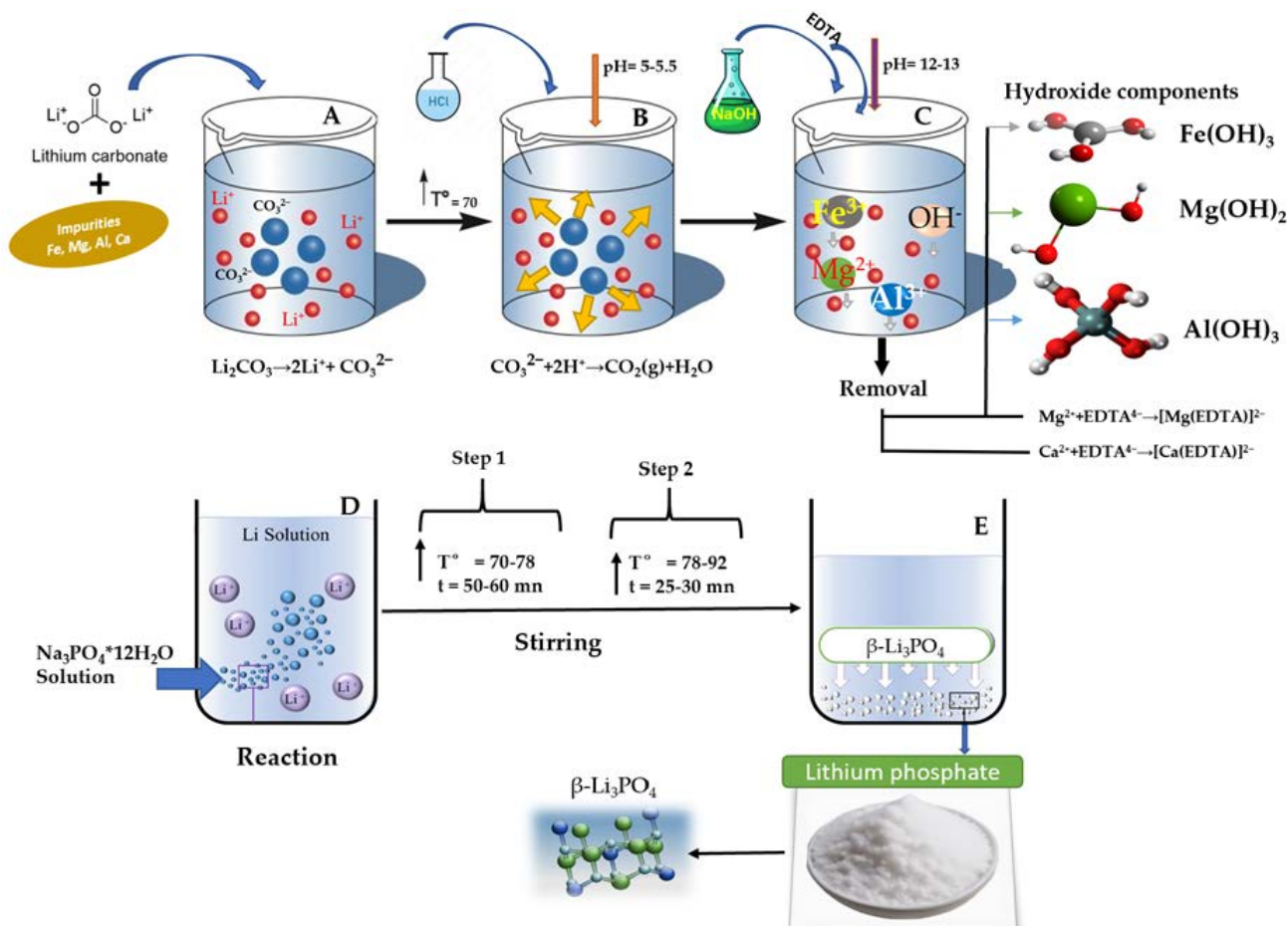


**Figure 3.** Lithium phosphate synthesis and raw materials impurities removal process.

During the increase in the lithium carbon solution's pH, some impurities such as Al, Fe, and Mg formed insoluble hydroxides in basic conditions and were removed from the solution. The added EDTA formed soluble complexes with  $\text{Mg}^{2+}$  and  $\text{Ca}^{2+}$  under vigorous stirring for 25–30 min and supported the precipitation of the remaining impurities.

The obtained solution was then filtered using a multifunction vacuum pump with water circulation and filter paper.

Secondly, an equivalent molarity of sodium phosphate source was dissolved in deionized water according to the following relationship:  $n[\text{Na}_3\text{PO}_4 \cdot 12\text{H}_2\text{O}] = n[\text{Li}^+]/3$ . The sodium phosphate solution was gradually added to the lithium source solution at 70–78 °C with vigorous stirring for 50–60 min. Additional heating and stirring for 25–30 min at 78–92 °C were necessary to complete the reaction, and a white precipitate ( $\text{Li}_3\text{PO}_4$ ) began to form immediately. The final white solution was filtered and washed; the solid phase was collected and dried at 105 °C for 2 h in an electrothermal fan dryer (Shanghai Lichen

Bangxi Instrument Technology Co., Ltd., Shanghai, China, No. 101-185). Table 2 presents the basic conditions of the process and statistics of the different samples.

**Table 2.** Basic conditions and statistics.

Samples	Li <sub>2</sub> CO <sub>3</sub>	Na <sub>3</sub> PO <sub>4</sub> .12H <sub>2</sub> O	pH Control Reagent	Reaction Temperature/°C	Reaction Time/min	pH	Li <sub>3</sub> PO <sub>4</sub> (g)	Yield (%)
LPO-1		9.942 g		78	40 min	12	2.40	79.19
LPO-2		9.942 g		78	50 min	12.5	2.37	78.20
LPO-3	3 g	9.942 g	HCl-NaOH	78–92	1 h 30 min	13	2.50	82.49
LPO-4		10 g		78–90	1 h 30 min	12.7	2.85	93.49

$$\text{yield}(\%) = \frac{\text{Experimental mass}}{\text{Theoretical mass}} \cdot 100; \text{ where Theoretical mass} = 3.04 \text{ to } 3.05 \text{ g.}$$

### 2.3. Sample Characterization Methods

Various techniques were used to characterize the different samples. The purity of the Li<sub>2</sub>CO<sub>3</sub> source and the content of impurities were determined using the standard titration method and inductively coupled plasma optical emission spectroscopy (ICP-OES) (Optima 5300 DV model, S09022867, manufacturing unit: PerkinElmer, USA).

The crystal phase studies for all samples were performed using the Empyrean Malv-inpanakry X-ray diffractometer (Goniometer reproducibility: 0.0001 degrees; controllable step: 0.0001 degrees; test voltage 45 kv 40 mA). All reflections were assigned using the International Center for Diffraction Data (ICDD).

The surface morphology of the particles and the distribution of the samples were characterized using scanning electron microscopy (SEM) (Company: Zeiss, Germany, Model: Sigma300) in combination with energy dispersive X-ray spectroscopy (EDS) (Oxford Energy Spectrograph 30 xplore).

X-ray photoelectron spectroscopy (XPS) was performed using ThermoFisher Scientific (America) with X-ray radiation of 10–400 μm (5 μm step size setting). The binding energies of the chemical elements were corrected with the internal standard C 1s (284.5 eV). The peaks were fitted with a Gaussian line shape in Origin 2024b software.

The electrochemical properties of the sample were analyzed by electrochemical impedance spectroscopy (EIS) using the DH7000 Electrochemical Workstation. The test was performed at room temperature, 40, 60, and 80 °C. The frequency was set to 1 MHz–0.01 Hz, and the amplitude to 5 mV. After the test, the EIS card was adjusted.

The atmospheric plasma spraying (APS, Jiangsu Donghua Analytical instrument Co., Ltd., Jiangyan, China) technique was used to deposit materials as coatings on surfaces with a surface area of 0.785 cm<sup>2</sup> and a thickness of 0.0781 cm measured with a spiral micrometer (model IP64). It used a symmetric cell with stainless steel blocking electrodes, with an amplitude of 10 mV and a frequency range of 0.1 to 1 MHz. This method consisted of measuring the conductivity from high temperature to room temperature to ensure the thermal stability of the sample. The ionic conductivity ( $\sigma$ ) of LPO-4 was calculated from the impedance data at RT, 40, 80 °C.

The thermal properties of the tested solid electrolyte were investigated using the TG/DTA7300 system (Seiko, Japon: Hitachi Corporation). The LPO-4 powder was heated to 820 °C under nitrogen supply at a rate of 10 °C min<sup>-1</sup>. Subsequently, the TG data were used to develop Coats and Redfern models using Plank and Boltzmann constants and to calculate the key kinetic and thermodynamic parameters for each thermal phase of the LPO-4 sample.

### 2.4. Modeling

We assumed that all conversions were first-order reactions. Coats and Redfern models were developed to calculate the kinetic and thermodynamic key parameters for each thermal phase, such as pre-exponential factor (A), Gibbs free energy changes ( $\Delta G$ ), entropy

changes ( $\Delta S$ ), and enthalpy changes ( $\Delta H$ ) [19–23]. The following equations and constants were used in this procedure:

$$\ln[-\ln(1-x)] = \ln \frac{ART^2}{\beta E_a} - \frac{E_a}{RT},$$

where:  $x = \frac{w_i-w_f}{w_i-w_f}$ ;  $w_i$ : initial sample weight;  $w_f$ : weight of sample at particular temperature T;  $w_f$ : final sample weight; A: pre-exponential factor;  $\beta$ : heating rate ( $10\text{ }^{\circ}\text{C}/\text{min}$ ); R: gas constant ( $8.3143\text{ Jmol}^{-1}\text{K}^{-1}$ );  $E_a$ : activation energy, T: temperature (K) at the peak of the DTG curves.

$$E_a = \text{slope} \times 8.3143$$

$$A = \frac{\beta E_a e^{\frac{E_a}{RT^2}}}{RT^2}$$

$$\Delta H = E_a - RT$$

$$\Delta G = E_a + T \cdot \ln \left( \frac{KT}{hA} \right)$$

$$\Delta S = \frac{\Delta H - \Delta G}{T}$$

where K is Boltzmann's constant ( $1.381 \times 10^{-23}\text{ J.K}^{-1}$ ), and h is Planck's constant ( $6.626 \times 10^{-34}\text{ J s}$ ).

The slope and intercept values of the plot of  $\ln[-\ln(1-x)]$  versus  $1000/T$  were used to determine the activation energies and other thermodynamic parameters.

### 3. Results and Discussion

#### 3.1. Lithium Mother Source Study

The lithium mother liquor ( $\text{Li}_2\text{CO}_3$ ) was first analyzed to understand its composition, purity, and water content. Titration is still one of the most popular and oldest methods for determining the purity of chemical components. The titration results of the different samples showed a purity of 96–97%.

Inductively coupled plasma mass spectroscopy indicates the presence of lithium and other impurities that were further removed during the treatment, as shown in Figure 3. The percentage and the concentration of each element were calculated using Equations (1) and (2), respectively, as presented in Table 3. The water content of lithium phosphate was calculated using Equation (3), as shown in Table 4.

$$\% \text{element} = C \cdot \frac{V_1}{m_{\text{Li}_2\text{CO}_3}} \cdot \frac{V_2}{V} \cdot 0.0001 \quad (1)$$

$$\text{concentration element (g/L)} = (C \cdot \frac{V_1}{m_{\text{Li}_2\text{CO}_3}} \cdot \frac{V_2}{V}) / (1000) \quad (2)$$

where,  $V_1 = 100\text{ mL}$ ,  $V_2 = 100\text{ mL}$ ,  $V = 2\text{ mL}$ ,  $m_{\text{Li}_2\text{CO}_3} = 0.507\text{ g}$ , and C (mg/L): concentration from ICP.

$$\% \text{ Water content} = [(A + B) - (C)]/B \quad (3)$$

**Table 3.** Composition of lithium carbonate.

$\text{Li}_2\text{CO}_3$				
Element	Intensity	Concentration (C) (mg/L)	with Equation (1) (%)	with Equation (2) (g/L)
Al	396.163	0.242	0.239	2.390
As	188.984	-0.320	-0.316	-3.163

**Table 3.** *Cont.*

Li <sub>2</sub> CO <sub>3</sub>				
Element	Intensity	Concentration (C) (mg/L)	with Equation (1) (%)	with Equation (2) (g/L)
B	249.778	−0.082	−0.081	−0.816
Ba	233.533	0.002	0.002	0.020
Bi	223.065	−0.009	−0.009	−0.096
Ca	317.941	0.358	0.353	3.531
Cd	214.443	−0.003	−0.003	−0.039
Cr	283.568	0.001	0.0015	0.015
Co	228.618	0.001	0.001	0.018
Cu	324.762	0.001	0.001	0.016
Fe	238.205	0.125	0.123	1.236
K	766.51	0.124	0.123	1.230
Li	670.803	18.460	18.205	182.059
Mg	285.217	0.134	0.132	1.323
Mn	257.615	0.011	0.011	0.110
Na	589.606	1.150	1.134	11.344
Ni	231.605	0.003	0.003	0.036
P	213.621	0.101	0.099	0.999
Pb	220.36	−0.009	−0.009	−0.097
Se	196.032	0.059	0.058	0.582
Sr	407.78	0.003	0.003	0.034
V	290.886	0.0006	0.0006	0.006
Zn	213.861	0.047	0.047	0.473

**Table 4.** Water content.

Sample	Weigh of Empty Glass (A)	Weigh of Sample (B)	(A + B)	Weigh After Drying (C)	Water Content (%)
Li <sub>2</sub> CO <sub>3</sub>	42.10	16	58.10	57.10	6.25

### 3.2. Impurities Removal Process and Their Distribution in Synthesized Samples

The preparation of lithium phosphate by co-precipitation of lithium carbonate (Li<sub>2</sub>CO<sub>3</sub>) and trisodium phosphate dodecahydrate (Na<sub>3</sub>PO<sub>4</sub>\*12H<sub>2</sub>O) has attracted great interest (simple and inexpensive). However, the challenge is the presence of some impurities that need to be removed or reduced to minimize their effects in the synthesized sample. As described in the previous section, these different steps cannot definitively remove some impurities. As can be seen in Figure 4, there were still traces of impurities in varying amounts in the samples due to the preparation conditions and severity. Since sodium is difficult to control, it was reduced from 1.26% in the first sample (LPO-1) to 0.28% in LPO-4 (only this sample was used to study ionic conductivity). Other impurities such as Al (0.03–0%), Ca (0.02–0%), Fe (0.01%), K (0.08–0.02) and Mg (0.02–0.01) were significantly reduced or eliminated. This performance in removing impurities was related to various factors, such as stirring of the solution, pH, amount of HCl, NaOH, and EDTA, as described in the “Experiment” section.

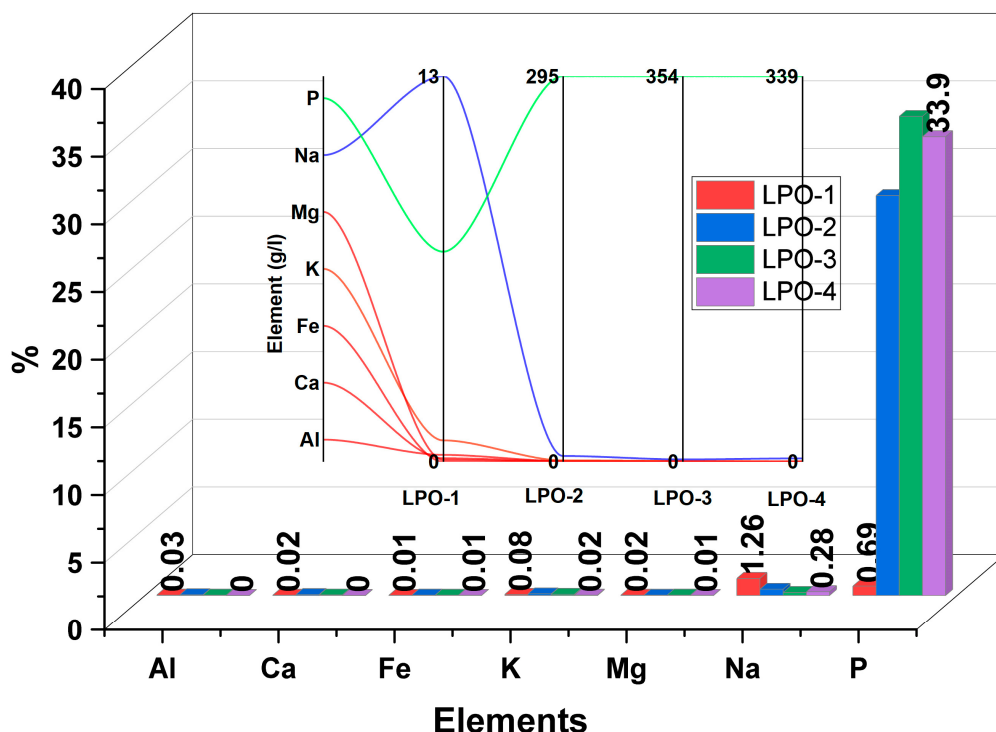


**Figure 4.** ICP analysis of element distribution in different samples.

### 3.3. Surfaces, Pore Distribution, and Isotherm ( $N_2$ ) Analysis

As can be seen from Table 5, the BET surface area ( $9.0293 \text{ m}^2 \text{ g}^{-1}$ ) is significantly lower than the Langmuir surface area ( $28.1896 \text{ m}^2 \text{ g}^{-1}$ ). This is because the BET method considers multilayer adsorption and provides a more conservative estimate compared to the Langmuir method, which assumes single-layer adsorption. The higher Langmuir value indicates that the sample has a significant amount of fine surface features that provide additional adsorption sites. On the other hand, the BET surface area ( $9.0293 \text{ m}^2 \text{ g}^{-1}$ ) is lower than the external t-plot surface area ( $19.6989 \text{ m}^2 \text{ g}^{-1}$ ). This is because BET measures the total accessible surface area, including contributions from micropores and mesopores, while the external t-plot surface area focuses on the surface area without micropores, suggesting that the sample has significant mesoporous and microporous structure. However, when the Langmuir and t-plot surface areas are compared, it is found that the Langmuir surface area is larger than the t-plot surface area. The Langmuir method tends to overestimate the surface area as it only takes into account the adsorption of single layers at all available sites, whereas the t-plot method provides a more realistic measure of the surface area accessible to larger molecules, excluding micropores.

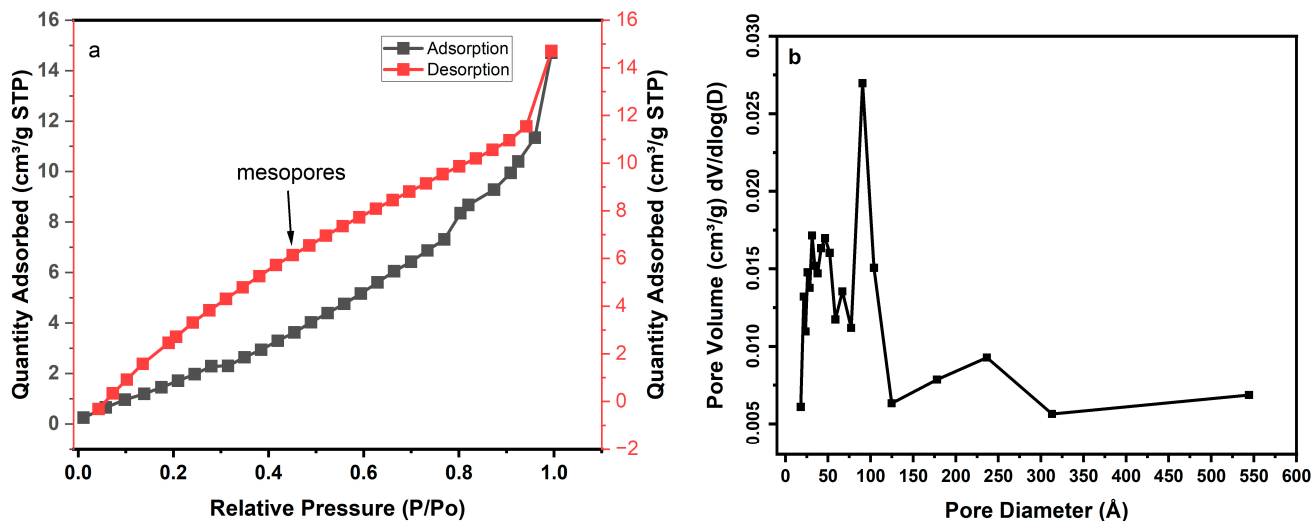
**Table 5.** LPO-4 properties.

Samples	$S_{\text{BET}}$ ( $\text{m}^2 \text{ g}^{-1}$ )	$S_{\text{t-Plot-Ext}}$ ( $\text{m}^2 \text{ g}^{-1}$ )	$S_{\text{Langmuir}}$ ( $\text{m}^2 \text{ g}^{-1}$ )	$V_{\text{total}}$ ( $\text{cm}^3 \text{ g}^{-1}$ )	$V_{\text{micro}}$ ( $\text{cm}^3 \text{ g}^{-1}$ )	Size
LPO-4	9.029	19.69	28.189	0.022	-	10.08 nm

The differences in these surface area measurements indicate the complex pore structure of the lithium phosphate sample. A higher Langmuir surface area indicates many fine pores, while a significant external t-plot surface area indicates a substantial contribution from larger mesopores and macropores. This balance is critical to understanding the material's potential applications in solid electrolytes, where both large surface area and appropriate pore sizes are important for ionic conductivity and structural integrity. The average BET

adsorption pore width (size) indicates a predominance of mesopores with an average width of 10.08 nm.

Figure 5a shows the isothermal  $N_2$  adsorption–desorption curve of the LPO-4 sample. The adsorption–desorption curve has characteristics similar to those of type IV, according to IUPAC rules [23]. The hysteresis loop appears above  $p/p_0 = 0.057$ , which represents a low-pressure point in the adsorption isotherm where mesoporous materials exhibit initial multilayer adsorption. The virtual absence of micropores is also observed.



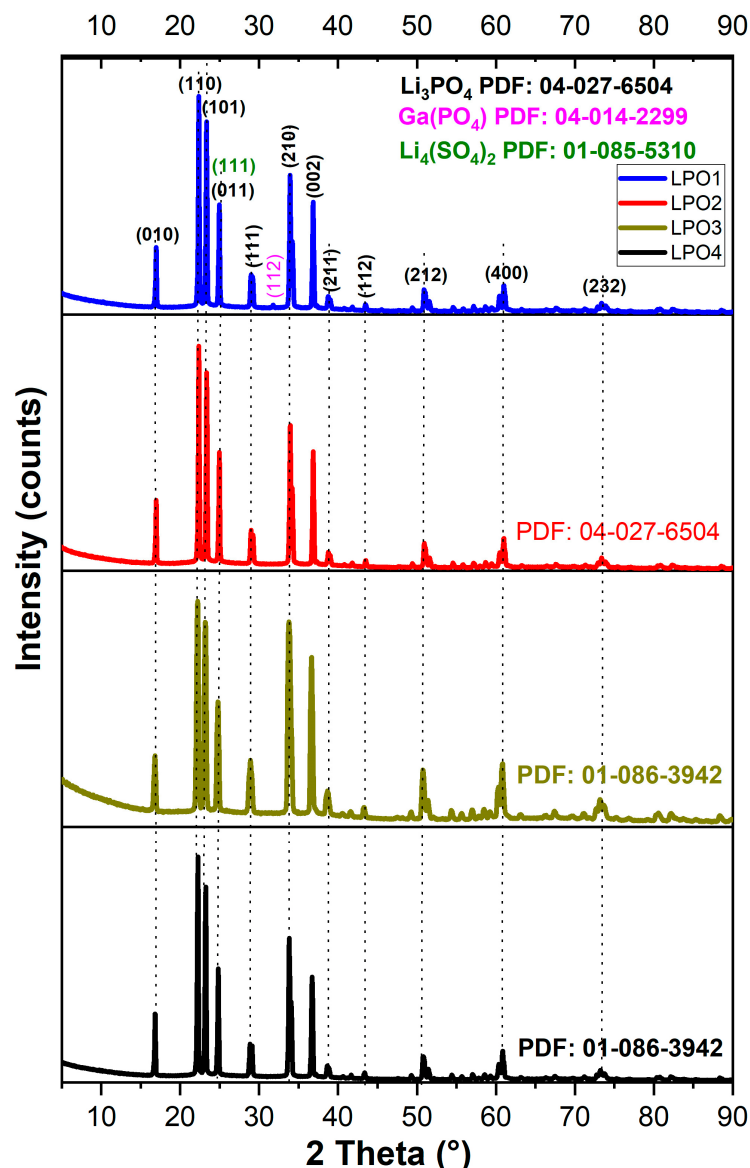
**Figure 5.** Isothermal adsorption–desorption curves (a) and the pore size distribution as the function of pore volume (b).

Figure 5b shows the particle size distributions as a function of the pore volume of LPO-4. From the observations in the figure and the table, the density of the small particles below 5 nm is important at a moderate pore volume compared to the particles above 10 nm. The 10 nm particles have a large pore volume, which increases the free ion transport and improves the sample's electrochemical performance.

### 3.4. Crystallography Analysis

The precipitation method is still available and simple to form a wide range of lithium phosphate structures and well-crystalline materials. In addition, the stoichiometric conditions, solution dissolution, stirring, time, and temperature of the preparation must be strict to ensure a good particle size distribution. Figure 6 shows the XRD patterns of the synthesized samples performed in the MDI Jade V9.1 software using WPF and the Rietveld refinement method. LPO-2, LPO-3, and LPO-4 spectrums reveal a single phase of  $\text{Li}_3\text{PO}_4$ , which agrees well with the patterns of lithium phosphate structure corresponding to the orthorhombic crystal system with space group  $\text{Pmn}21$  (31) (PDF of 04-027-6504 and 01-086-3942) [10,24]. In all samples, the diffraction peaks appeared at close positions of 16.9, 22.32, 23.37, 24.98, 28.99, 36.99, 38.78, 43.64, 51.06, 60.08, 60.51, 73.58°, corresponding to the reflections (010), (110), (101), (011), (111), (002), (211), (112), (212), (222), (400), and (232) planes. However, the spectrum of LPO-1 shows lithium phosphate as the main phase and two other phases of gallium phosphate ( $\text{Ga}(\text{PO}_4)$ ) with a weak intensity peak of  $2\theta \approx 31.77^\circ$  and  $\text{Li}_4(\text{SO}_4)_2$  with a peak of  $2\theta \approx 25.86^\circ$ , corresponding to the reflections (112) and (111) planes, (PDF: 04-014-2299 and 01-085-5310) [25,26]. The formation of the  $\text{Ga}(\text{PO}_4)$  phase of 0.1% probably comes from other reagents used in the process, while the formation of 0.2%  $\text{Li}_4(\text{SO}_4)_2$  phase may attributed to the lithium reach and the synthesis conditions as presented in the experience and XPS analysis sections. As shown in Table 6, the calculations of the XRD data revealed the amount and the lattice constants of the individual phases

formed in the different samples. The LPO-2, LPO-3, and LPO-4 samples showed a single phase (100%) of  $\beta$ -Li<sub>3</sub>PO<sub>4</sub>, as shown in Figure 7 (left).



**Figure 6.** XRD patterns of samples LPO1, LPO2, LPO3, and LPO4.

**Table 6.** Calculated lattice Constants of samples.

Samples	Phase	a (Å)	b (Å)	c (Å)	Cell Volume (Å <sup>3</sup> )	Density (g/cm <sup>3</sup> )
LPO-1	$\beta$ -Li <sub>3</sub> PO <sub>4</sub>	6.115	5.2394	4.855	155.56	2.472
LPO-2	$\beta$ -Li <sub>3</sub> PO <sub>4</sub>	6.115	5.2394	4.854	155.56	2.471
LPO-3	$\beta$ -Li <sub>3</sub> PO <sub>4</sub>	6.115	5.2394	4.854	155.56	2.471
LPO-4	$\beta$ -Li <sub>3</sub> PO <sub>4</sub>	6.115	5.2394	4.854	155.56	2.471

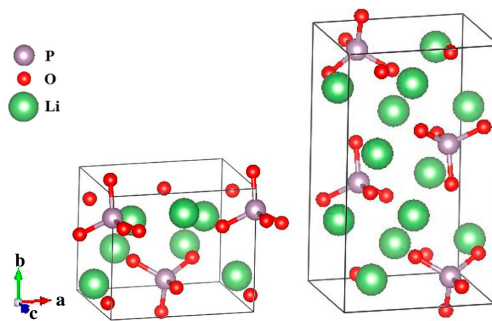


**Figure 7.** Crystal structure of  $\beta$ -Li<sub>3</sub>PO<sub>4</sub> (left) and  $\gamma$ -Li<sub>3</sub>PO<sub>4</sub> (right) [10].

### 3.5. Morphology and Impurities Distribution Analysis (SEM-EDS and ICP-OES)

Figure 8 shows the SEM images of samples LPO-1, LPO-2, LPO<sub>3</sub>, and LPO-4, which were prepared from lithium carbonate and trisodium phosphate dodecahydrate at different pH values and temperatures. All samples exhibited irregular (rectangular) nanotube shapes. A comparison of the observations revealed that the particle shapes of LPO-1 (pH = 12) may be due to an incomplete reaction during production. LPO-2 (pH = 12.5), LPO-3 (pH = 13), and LPO-4 (pH = 13) exhibited complete particle shapes with spherical, cross-linked small particles, with average small particle sizes increasing between 2–100 nm. In the bulk of the samples, LPO-4 showed high purity with a trace of the element sodium (0.28–0.22%, 2.88 g/L), confirmed by coupled plasma mass spectroscopy (ICP) and energy dispersive X-ray spectroscopy (EDS) analysis, as shown in Figures 4 and 9, respectively.

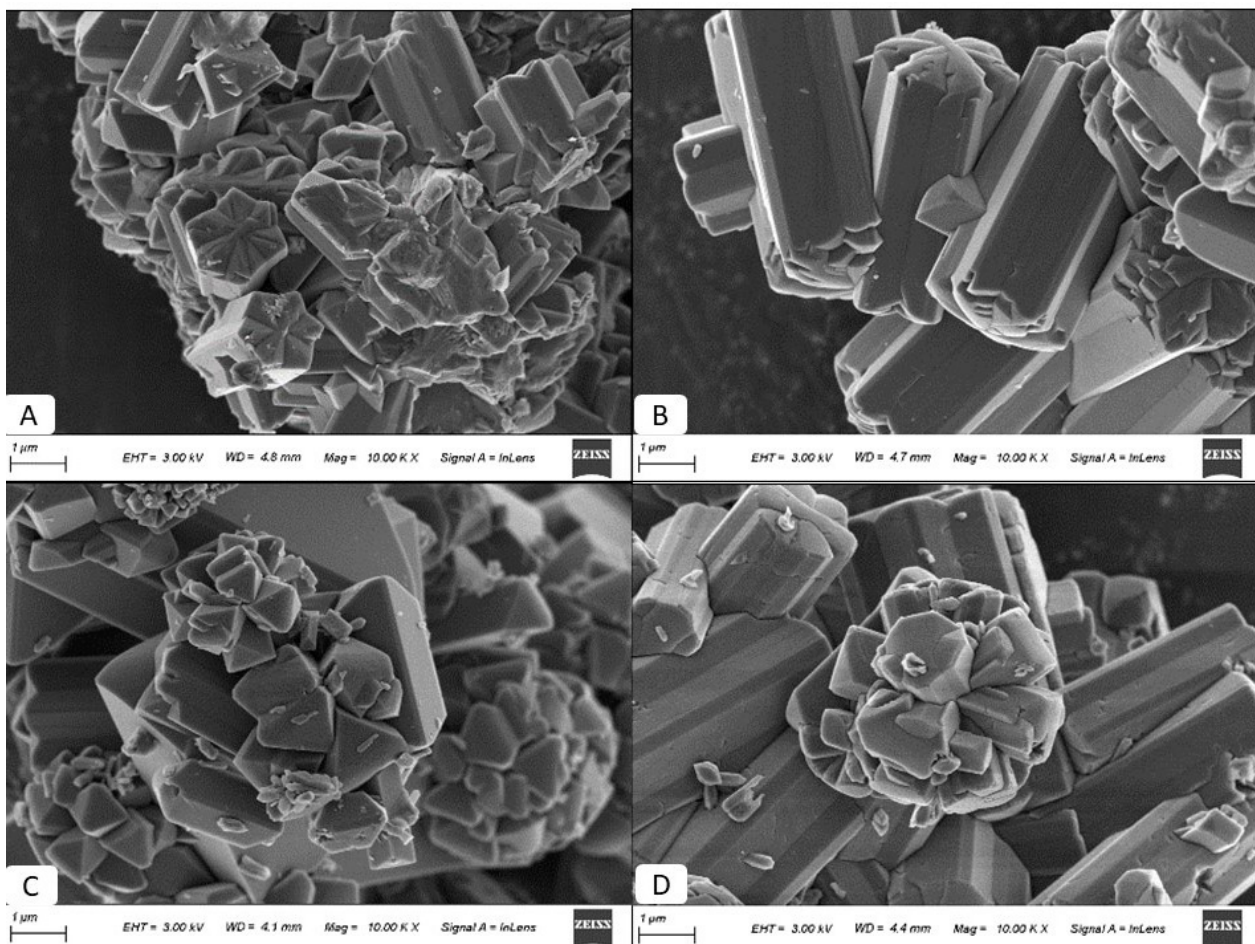


**Figure 8.** SEM images of (A) (LPO-1), (B) (LPO-2), (C) (LPO-3), and (D) (LPO-4).

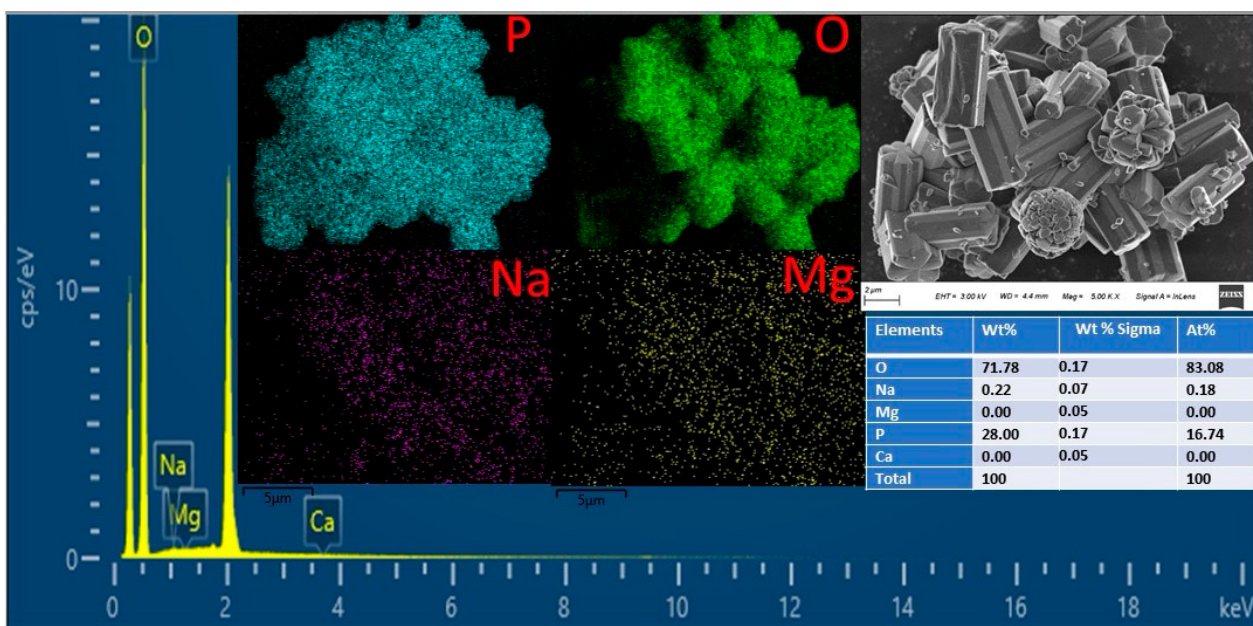


**Figure 9.** Energy Dispersive X-ray Spectroscopy (EDS) of LPO-4 sample—purities distribution.

### 3.6. X-Ray Photoelectron Analysis

The X-ray photoelectron (XPS) analysis was investigated to determine the main elements bending energies, their atomic concentration, and ratio in the material. XPS is known to be a powerful technique that can provide a surface analysis with specific information about bonding between atoms and their oxidation in the material.

Table 7 shows the elemental states of lithium, phosphate, and oxygen and their atomic compositions, which were analyzed using X-ray photoelectron spectroscopy (XPS). In both samples, the atomic ratios of Li/P and O/P were close to the stoichiometric values of 3 and 4, respectively. These slight deviations from the stoichiometric values could be due to the slight excess of lithium and oxygen atoms compared to the ideal ratios. The bending energy values of Li 1s, P 2p, and O 1s of all samples were similar and close, as shown in Table 7. On the other hand, these values are in good agreement with those reported by Tae Yong Kim [1]. The atomic ratio of Na/P of all samples was also calculated to determine the degree of sample purities and understand their impact on the chemical environment as the main impurity. The LPO-4 presents the lowest Na/P ratio of 0.06 against 0.84, 0.66, and 0.52 for LPO-1, LPO-2, and LPO-3, respectively. Because of its lowest Na atomic concentrations (0.67% atomic), LPO-4 was considered as a reference to compare the local electronic environment of C 1s, Li 1s, P 2p, O 1s, and Na 1s species in different samples.

**Table 7.** Sample elements' binding energies and atomic ratios.

		LPO-1	LPO-2	LPO-3	LPO-4
Binding Energy (eV)	Li 1s	54.8	54.8	54.7	54.8
	P 2p	133.0	133.05	133.0	133.1
	O 1s	530.9	530.87	530.9	531.0
	C 1s	284.8	284.8	284.8	284.7
	Na 1s	1071.4	1071.4	1071.6	1071.8
Atomic ratio	Li/P	3.1	3.2	3.0	3.0
	O/P	4.3	4.3	4.2	4.1
	Na/P	0.84	0.66	0.52	0.06

Figure 10 shows C 1s, Li 1s, P 2p, O 1s, and Na 1s spectra, elements, and bending energies (as shown in Table 8) of various samples. For all samples, Li 1s spectra exhibited a major peak at 54.84 eV attributed to  $\text{Li}_2\text{CO}_3$ , which may originate from the lithium mother

liquor source. LPO-1 showed an additional smaller  $\text{Li}_2\text{CO}_3$  peak in the Li-1s spectra at the same position as the first peak. Observation shows that the intensity of the main peak of  $\text{Li}_2\text{CO}_3$  decreases from LPO<sub>1</sub> to LPO-4, indicating the decrease in its concentration due to the stoichiometric approach to the ideal values (Li/P).

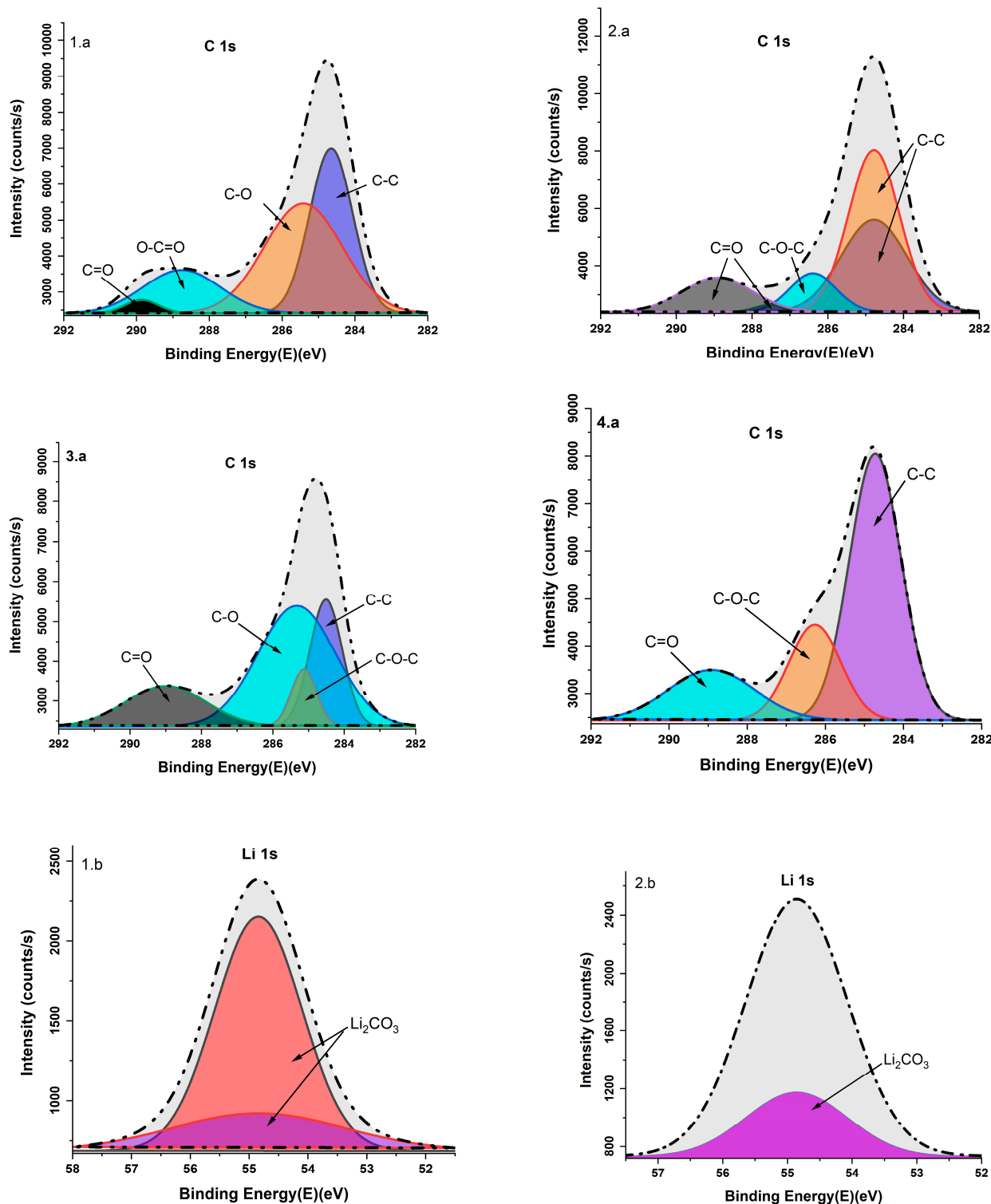
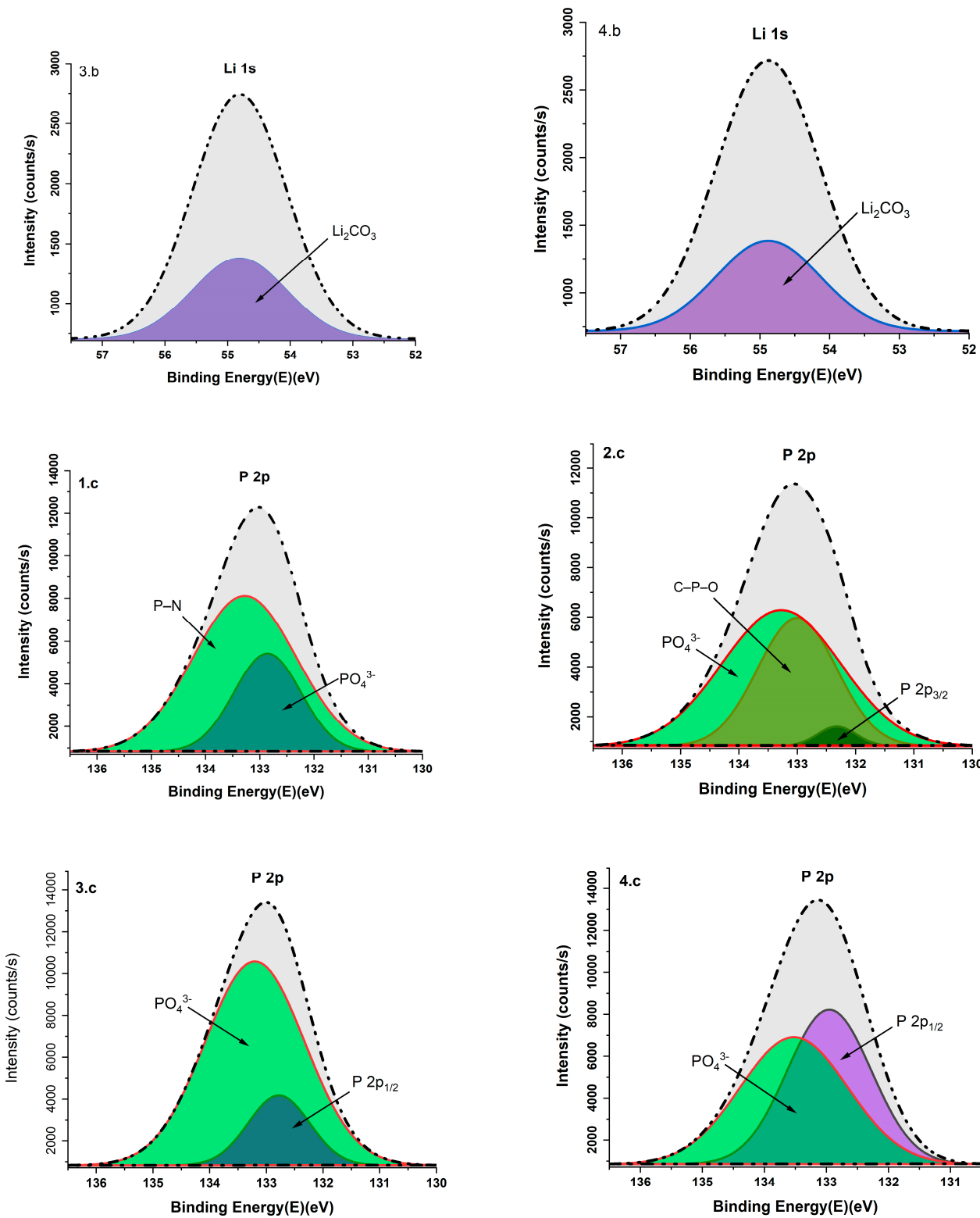


Figure 10. Cont.



**Figure 10. Cont.**

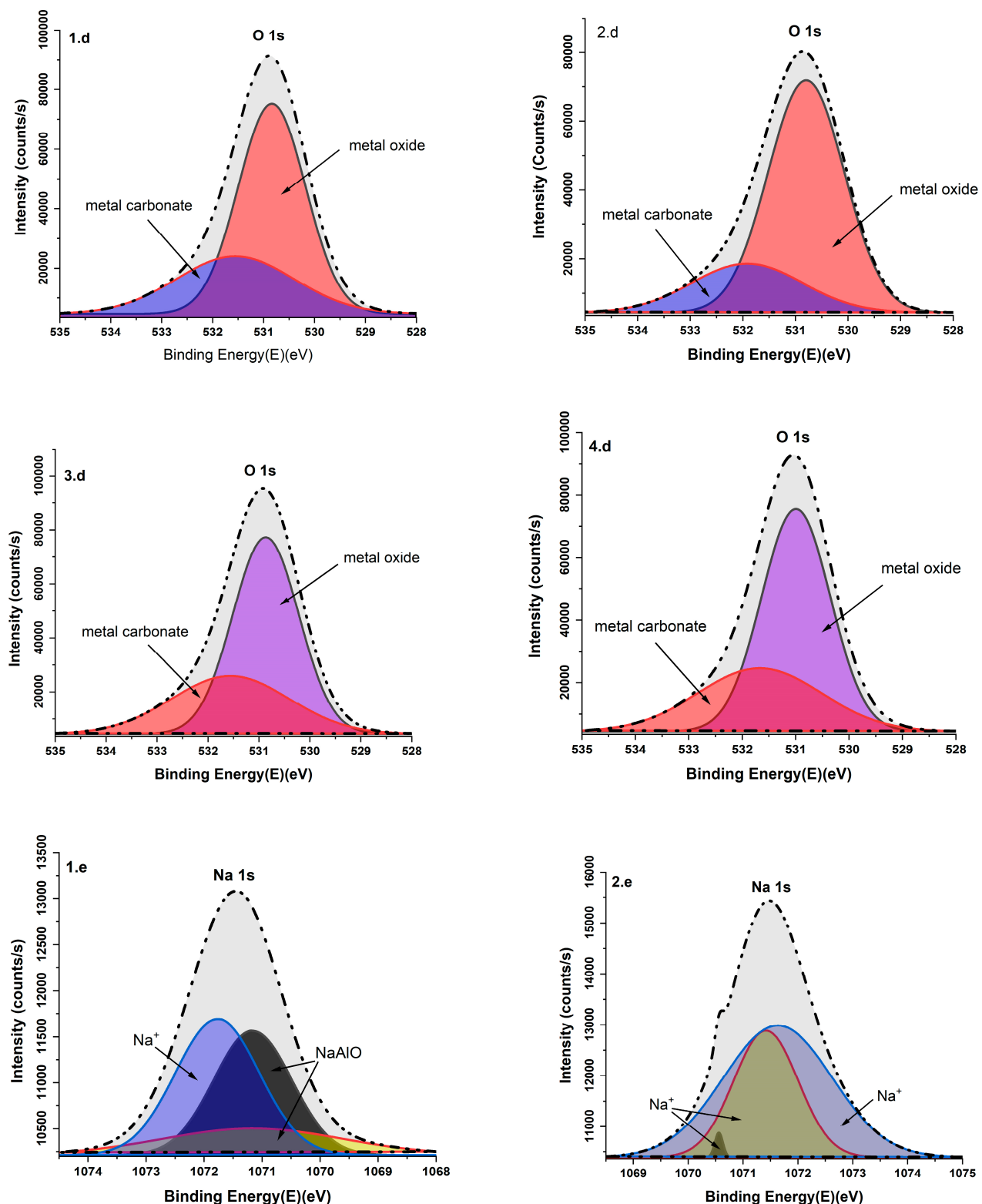
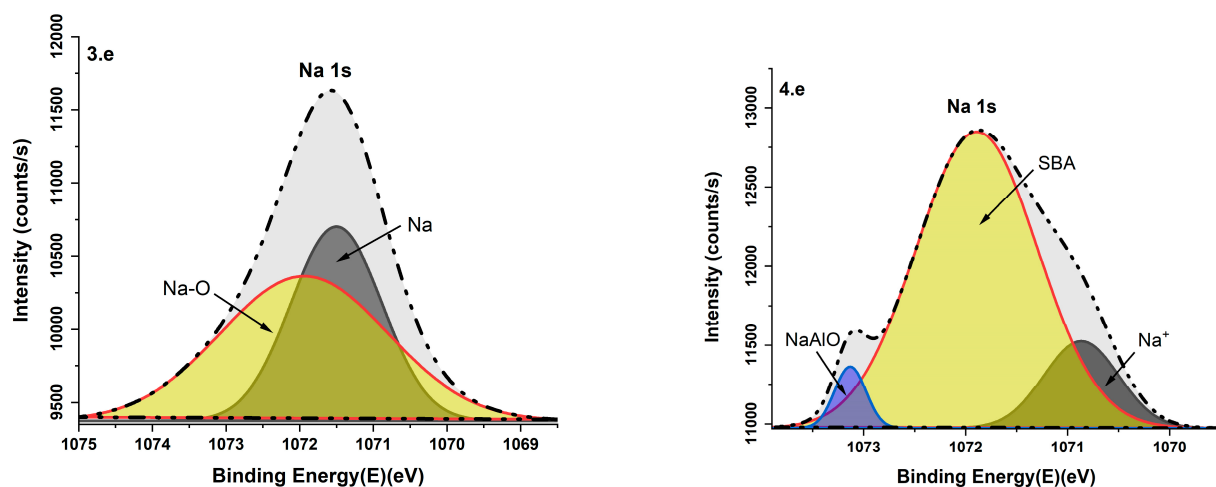


Figure 10. Cont.



**Figure 10.** XPS C 1s, Li 1s, P 2p, O 1s, and Na 1s core spectra for LPO-1 (1.a, 1.b, 1.c, 1.d, and 1.e), LPO-2 (2.a, 2.b, 2.c, 2.d, and 2.e), LPO-3 (3.a, 3.b, 3.c, 3.d, and 3.e), and LPO-4 (4.a, 4.b, 4.c, 4.d, and 4.e).

**Table 8.** XPS peak Binding Energies and Assignments.

Spectra	Binding Energy (eV)	Assignment	Refs.
C 1s	284.65/284.50/284.72	C-C	[27,28]
	285.41/285.32	C-O	[29,30]
	288.75	OC=O	[27]
	289.00/289.85	C=O	[27,31]
	285.12/286.26	C-O-C	[27]
Li 1s	54.84	$\text{Li}_2\text{CO}_3$	[32]
	133.27	P-N	[33]
	132.77/132.95	$\text{P } 2\text{p}_{1/2}$	[34,35]
P 2p	133.27/133.52/133.20/132.85	$\text{PO}_4^{3-}$	[36–38]
	132.32	$\text{P } 2\text{p}_{3/2}$	[39]
	133.00	C-P-O	[40]
O 1s	531.56	metal carbonate	[41]
	530.86	metal oxide	[41]
Na 1s	1071.7/1070.86	$\text{Na}^+$	[42]
	1071.16/1073.13	Sodium oxides ( $\text{NaAlO}$ )	[43]
	1071.89	SBA	[44]
	1071.94	Na-O	[45]
	1071.50	Na	[46]

The P 2p peaks of  $\text{PO}_4^{3-}$  were identified in all samples with slight shifts at 133.2 eV for LPO-4/LPO-2 and at 132.85 eV and 133.5 eV for LPO-1 and 3, respectively. The P 2p spectra of LPO-1 showed a peak at 133.27 eV, which was assigned to the P-N species. The P 2p spectra showed a peak of the  $\text{P } 2\text{p}_{1/2}$  species at 132.77 and 132.95 eV for LPO-4 and 3, respectively. The additional LPO-2 P 2p peaks identified at 133.00 eV and 132.32 eV were assigned to C-P-O and  $\text{P } 2\text{p}_{3/2}$ , respectively. However, the surface areas and intensities of the O 1s peaks were similar for all samples, with a slight shift. The peaks at 530.86 and 531.56 eV correspond to metal oxide (possibly  $\text{Li}_2\text{O}$ ) and metal carbonate, respectively.

The C 1s XPS core spectra showed peaks with slight shifts attributable to C-C bonds at 284.65, 284.77, 284.50, and 284.72 eV in LPO-1, 2, 3, and 4, respectively. Additional peaks of 286.39, 285.12, and 286.26 eV were found in LPO-2, 3, and 4, respectively. These C 1s peaks corresponded to the C-0-C species. The C=O binding energy at 289.85 eV for LPO-1, 287.53–288.91 eV for LPO-2, 289.00 for LPO-3 and 288.91 eV for LPO-4. The O-C=O binding energy at 288.75 eV was found only in the LPO-1 C1s spectra, while two other binding energies at 285.41 and 285.12 eV were found in LPO-1 and 3, which correspond to the C-O environment due to the carbon layer on most of the sample surfaces exposed to air. The carbon peaks of the samples originate from surface impurities.

The XPS spectrum of Na 1s in LPO<sub>4</sub> is decomposed into two peaks at 1070.77 and 1073.13 eV, indicating the presence of Na<sup>+</sup>. The Na 1s peaks in LPO<sub>3</sub> with binding energies of 1071.50 and 1071.94 eV indicate the presence of Na and Na-O, respectively.

The same Na 1s peak of Na<sup>+</sup> was found at 1071.16, 1071.16, and 1071.77 eV for LPO-2 and 1071.63 eV. An additional Na 1s peak of sodium oxides (NaAlO) was found at 1070.55 and 1071.41 eV in LPO-1 and at 1073.131 eV in LPO-4. The XPS spectrum of LPO-4 for Na 1s showed another peak at 1071.89 eV, indicating the presence of SBA species in the sample structure.

As can be seen in Figure 10, LPO-4 exhibited clear and strong peaks of C 1s, Li 1s, P 2p, and O 1s, indicating that this sample may have more stable solid electrolytes. Other slight changes in peak positions or intensities could be related to the slight variations in particle structure (e.g., slight disorder or variations in crystal quality) of the different samples (as shown in Figure 8), which may affect the electronic structure of the elements, resulting in shifts in the observed binding energies. The change may also originate from the local chemical environment around the lithium, phosphorus, and oxygen atoms, which is essentially due to residual impurities in LPO-1, LPO-2, and LPO-3 samples.

### 3.7. Electrical Properties

Figure 11a shows the Nyquist plot curves of lithium phosphate (LPO-4, pH = 13) at different temperatures (room temperature, 40, 60, and 80 °C). The spectra were obtained in a frequency range of  $f = 0.01$  Hz to 1 MHz. A clear semicircle was identified in the high-frequency range, and the Warburg impedance line was identified in the low-frequency range.

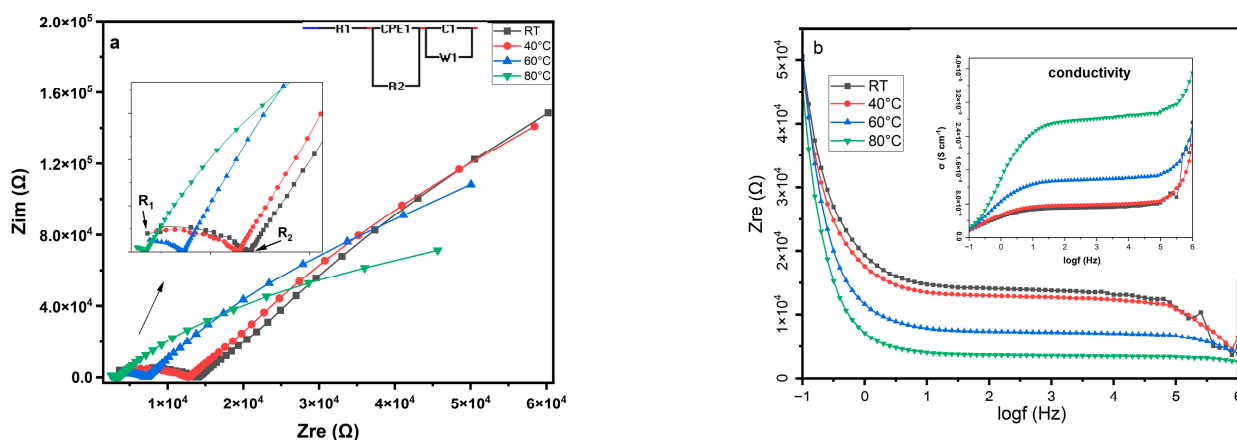


**Figure 11.** (a) The Nyquist plot of LPO-4 and the equivalent experimental circuit; (b) resistivities and ionic conductivities as a function of frequencies ( $\log f$  (Hz)).

The first resistance ( $R_1$ ) was interpreted as the bulk's response to the electric field. The second resistance ( $R_2$ ) could indicate additional resistances, such as grain boundary resistance or secondary interfacial processes of the sample.

An electrical circuit containing three resistors, a constant phase (CPE1), a capacitor, and an open Warburg, which was associated with lithium-ion diffusion, was proposed for

the electrical analysis. The following formula was used to determine the ionic conductivity of the sample:  $\sigma = L/(R \cdot A)$

Where: L is the thickness of the pellets in cm, R is the bulk resistance in  $\Omega$ , and A is the paste area of the sample in  $\text{cm}^2$ . The intersection of the semicircle with the high-frequency region was used to determine the total resistance, which corresponds to the  $R_2$  of the circle. The ionic conductivities obtained were  $7.1 \times 10^{-6} \text{ S.cm}^{-1}$  at room temperature,  $7.6 \times 10^{-6} \text{ S.cm}^{-1}$ ,  $1.3 \times 10^{-5} \text{ S.cm}^{-1}$ , and  $2.7 \times 10^{-5} \text{ S.cm}^{-1}$  at 40, 60 and 80 °C, respectively. As presented in Figure 11b, these values were higher than  $\text{Li}_3\text{PO}_4$  conductivity values of  $1.8 \cdot 10^{-10} \text{ S.cm}^{-1}$  and  $4.65 \times 10^{-8} \text{ S.cm}^{-1}$ ,  $3.10^{-7} \text{ S.cm}^{-1}$ , and  $4.10^{-8} \text{ S.cm}^{-1}$  reported by Lucas Dwi Prayogi et al. [3], Yin-Qiu Sun et al. [2], and Nur I.P. Ayu et al. [10], respectively. This performance in conductivity may be attributed to the short diffusion distance of lithium ions due to the particle nanoscales and nanotube morphologies with high surface area ( $9.029 \text{ m}^2\text{g}^{-1}$ ).

### 3.8. Kinetic and Thermodynamic Analysis

Figure 12 shows the thermogravimetric (TG) profile and a derived thermogravimetric (DTG) profile as a function of temperature. The TG curve shows the mass loss profile with increasing temperature, while the DTG curve shows two small and strong endothermic peaks at 222.7 and 450 °C. These peaks may correspond to decomposition processes. These peaks can be assigned to the decomposition phases of the sample from its original structure.

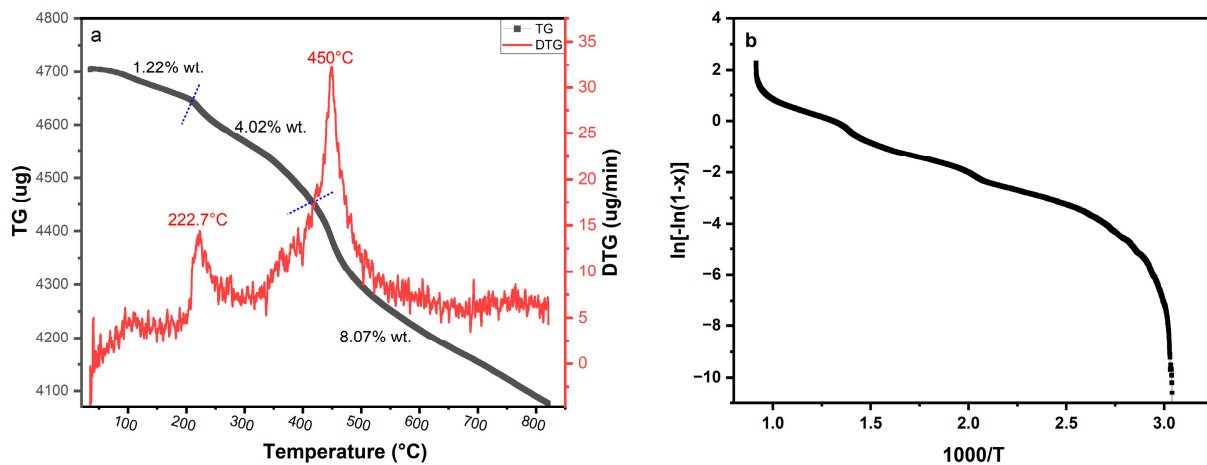


**Figure 12.** (a): Thermal phases and (b): plot of  $\ln[-\ln(1-x)]$  over  $1000/T$ .

The sample, with its key kinetic and thermodynamic parameters, provided important insights into the thermal stability and decomposition behavior of LPO-4 ( $\beta\text{-Li}_3\text{PO}_4$ ). The data were divided into three different phases, each characterized by specific temperature ranges, weight loss percentages, activation energies (E<sub>a</sub>), and thermodynamic parameters ( $\Delta S$ ,  $\Delta H$ , and  $\Delta G$ ), as shown in Table 9. These parameters are crucial for understanding the stability of the material and its potential performance as a solid electrolyte in lithium batteries, pointing the way for further investigations.

**Table 9.** Kinetic and thermodynamic parameters of LPO-4.

Phases	T °C Range	Loss (Wt.%)	Ea (eV)	ΔS	ΔH	ΔG	Fitting Equations	A (M.s <sup>-1</sup> )
1	RT–208.7 °C	1.22	0.38	−206.502	$1.49 \times 10^{+8}$	$1.49 \times 10^{+8}$	$Y = -4.4647x + 7.498$ $R^2 = 80.56$	163.89
2	208.7–414.8 °C	4.02	0.19	−261.54	$1.1 \times 10^{+8}$	$1.1 \times 10^{+8}$	$Y = -2.3067x + 2.608$ $R^2 = 98.92$	0.31
3	414.8–820.89 °C	8.07	0.29	−255.374	$2.58 \times 10^{+8}$	$2.58 \times 10^{+8}$	$Y = -3.4057x + 4.352$ $R^2 = 95.09$	1.04

The first phase was measured at room temperature up to 208.7 °C. This phase exhibits relatively low weight loss and moderate activation energy (0.38 eV). This loss can be related to the removed moisture in the sample (RT–208.7 °C). The negative entropy change ( $\Delta S$ ) indicates a decrease in disorder in this phase. The higher pre-exponential factors in the first phase lead to more frequent effective collisions and reactions, reflecting the efficiency of LPO-4 in facilitating ion movement in this region.

The second phase was defined in the temperature range of 208.7–414.8 °C. In this phase, a higher weight loss indicates a stronger decomposition, and the activation energy decreases to 0.19 eV. The more negative  $\Delta S$  value indicates a greater decrease in disorder.

The third phase shows the highest weight loss, indicating a significant decomposition of the material. The activation energy ( $E_a = \text{slope} \times 8.3143$ ) increases slightly to 0.29 eV compared to the second phase, indicating a certain resistance of the bonds and a degree of thermal stability, which is still relatively low. The entropy change ( $\Delta S$ ) remains negative. The high values for enthalpy change ( $\Delta H$ ) in the first and third phases indicate that the material is relatively stable and requires significant energy to decompose; thus, it may be suitable for applications requiring high thermal stability. The activation energies for all phases are below 5 eV and relate to the values for superionic conductors [47,48]. The  $R^2$  values for all phases show a strong correlation between the experimental data and the fitting model.

#### 4. Conclusions

Solid lithium phosphate electrolyte samples with the formula ( $\text{Li}_3\text{PO}_4$ ) were synthesized from lithium carbonate ( $\text{Li}_2\text{CO}_3$ ) and trisodium phosphate dodecahydrate ( $\text{Na}_3\text{PO}_4 \cdot 12\text{H}_2\text{O}$ ) by co-precipitation at different pHs, temperatures, and stoichiometric values. A single-phase, high-purity and ionically conductive  $\beta$ - $\text{Li}_3\text{PO}_4$  with nanotube morphologies was successfully prepared in the set of samples at 90 °C and pH 13. The ionic conductivities obtained were  $7.1 \times 10^{-6} \text{ S.cm}^{-1}$  at room temperature,  $7.6 \times 10^{-6} \text{ S.cm}^{-1}$ ,  $1.3 \times 10^{-5} \text{ S.cm}^{-1}$ , and  $2.7 \times 10^{-5} \text{ S.cm}^{-1}$  at 40, 60, and 80 °C, respectively.

The LPO-4 sample exhibited excellent electrochemical properties and represents a promising route for the further industrial application of lithium phosphate as a sustainable and environmentally friendly solid electrolyte. The actual achievement compared with some previous work on lithium phosphate, including its conductivity, high surface area, and lower activation energy, may be attributed to nanotubes and nanoscale size of the synthesized LPO-4, which enlarge the reaction interfaces and shorten the diffusion distance of lithium ions.

The kinetic and thermodynamic studies confirmed the excellent stability in the temperature range RT–208 °C and some endothermic reactions that can occur in high-temperature ranges.

**Author Contributions:** Conceptualization, S.Y.Z.; Methodology, S.Y.Z.; Software, S.Y.Z.; Validation, S.Y.Z., H.Y. and C.J.; Formal analysis, S.Y.Z.; Investigation, S.Y.Z.; Resources, S.Y.Z. and H.Y.; Data curation, S.Y.Z.; Writing—original draft, S.Y.Z.; Writing—review & editing, S.Y.Z. and C.J.; Visualization, S.Y.Z.; Supervision, H.Y.; Project administration, S.Y.Z., H.Y. and C.J.; Funding acquisition, H.Y. All authors have read and agreed to the published version of the manuscript.

**Funding:** This research was funded by National Natural Science Foundation project 21975288.

**Data Availability Statement:** The data presented in this study are available on request from the authors.

**Conflicts of Interest:** The authors declare no conflict of interest.

#### References

1. Kim, T.Y.; Song, C.K.; Yun, Y.S.; Yun, D.; Han, J.W.; Yi, J. Active site structure of a lithium phosphate catalyst for the isomerization of 2,3-epoxybutane to 3-buten-2-ol. *Mol. Catal.* **2018**, *445*, 133–141. [[CrossRef](#)]
2. Sun, Y.Q.; Luo, X.T.; Zhu, Y.S.; Liao, X.J.; Li, C.J.  $\text{Li}_3\text{PO}_4$  electrolyte of high conductivity for all-solid-state lithium battery prepared by plasma spray. *J. Eur. Ceram. Soc.* **2022**, *42*, 4239–4247. [[CrossRef](#)]

3. Prayogi, L.D.; Faisal, M.; Kartini, E.; Honggowiranto, W. Supardi, Morphology and conductivity study of solid electrolyte Li<sub>3</sub>PO<sub>4</sub>. *AIP Conf. Proc.* **2016**, *1710*, 030047. [CrossRef]
4. Fan, L.; Wei, S.; Li, S.; Li, Q.; Lu, Y. Recent Progress of the Solid-State Electrolytes for High-Energy Metal-Based Batteries. *Adv. Energy Mater.* **2018**, *8*, 1702657. [CrossRef]
5. Rosen, M.; Hecker, P.; Mann, M.; Ma, Q.; Gross, J.P.; Schwaiger, R.; Guillon, O.; Fattakhova-Rohlfing, D.; Finsterbusch, M. Reducing the environmental footprint of solid-electrolytes—A green synthesis route for LATP. *Green Chem.* **2024**, *26*, 2712–2720. [CrossRef]
6. Saran, S.; Eker, Y.R. Synthesis, structural and conductive properties of Nd doped garnet-type Li<sub>7</sub>La<sub>3</sub>Zr<sub>2</sub>O<sub>12</sub> Li-ion conductor. *Curr. Appl. Phys.* **2022**, *41*, 1–6. [CrossRef]
7. Xiao, B.; Li, D.; Dai, X.; Wei, Y.; Liao, Y.; Wang, C.; Ji, F.; Wu, F. Construction of a robust lithium cobalt phosphate layer for enhancement of the electrochemical performance of LiNi<sub>0.8</sub>Co<sub>0.1</sub>Mn<sub>0.1</sub>O<sub>2</sub> at high voltage. *Electrochim. Acta* **2024**, *475*, 143648. [CrossRef]
8. Zeng, S.; Ding, X.; He, L.; Li, H.W.; Zhang, Q.; Li, Y. Realizing fast Li-ion conduction of Li<sub>3</sub>PO<sub>4</sub> solid electrolyte at low temperature by mechanochemical formation of lithium-containing dual-shells. *Mater. Adv.* **2023**, *4*, 2780–2784. [CrossRef]
9. Kuwata, N.; Iwagami, N.; Matsuda, Y.; Tanji, Y.; Kawamura, J. Thin Film Batteries with Li<sub>3</sub>PO<sub>4</sub> Solid Electrolyte Fabricated by Pulsed Laser Deposition. *ECS Trans.* **2009**, *16*, 53–60. [CrossRef]
10. Ayu, N.I.P.; Kartini, E.; Prayogi, L.D.; Faisal, M. Supardi, Crystal structure analysis of Li<sub>3</sub>PO<sub>4</sub> powder prepared by wet chemical reaction and solid-state reaction by using X-ray diffraction (XRD). *Ionics* **2016**, *22*, 1051–1057. [CrossRef]
11. Zhao, S.; Jiang, W.; Zhu, X.; Ling, M.; Liang, C. Understanding the synthesis of inorganic solid-state electrolytes for Li ion batteries: Features and progress. *Sustain. Mater. Technol.* **2022**, *33*, e00491. [CrossRef]
12. Method for Recovering Lithium from Lithium Carbonate Precipitation Mother Liquor. CN111533146A. Available online: <https://patents.google.com/patent/CN111533146A/zh> (accessed on 25 October 2024).
13. Liu, W.Y.; Li, C.L.; Fu, Z.W. Stability of Nitrogen-Containing Lithium Phosphate Films in Air. *Acta Phys.-Chim. Sin.* **2006**, *22*, 1413–1418. Available online: [https://qikan.cqvip.com/Qikan/Article/Detail?id=23426027&from=Qikan\\_Article\\_Detail](https://qikan.cqvip.com/Qikan/Article/Detail?id=23426027&from=Qikan_Article_Detail) (accessed on 2 October 2024).
14. Wu, J. Discussion on the process of preparing lithium dihydrogen phosphate from lithium phosphate tower skin. *XinJiang Youse Jinshu* **2012**, *S1*, 124–125. Available online: [https://qikan.cqvip.com/Qikan/Article/Detail?id=1003444489&from=Qikan\\_Article\\_Detail](https://qikan.cqvip.com/Qikan/Article/Detail?id=1003444489&from=Qikan_Article_Detail) (accessed on 2 October 2024).
15. Wu, S.; Zhang, M.; Zan, C.; Zhou, H. Process of Deep Recovery of Lithium from the Mother Liquor of Lithium Carbonate by Phosphate Precipitation. *J. Tianjin Univ. Sci. Technol.* **2023**, *38*, 35–41. [CrossRef]
16. Yao, X.; Wang, Y.; Xu, M.; Shuying, S.U.N. Preparation of lithium phosphate from waste liquid of retired lithium batteries. *Chem. Ind. Eng.* **2024**, *41*, 179–190. [CrossRef]
17. Ishigaki, N.; Akimoto, J. Room temperature synthesis and phase transformation of lithium phosphate Li<sub>3</sub>PO<sub>4</sub> as solid electrolyte. *J. Asian Ceram. Soc.* **2021**, *9*, 452–458. [CrossRef]
18. Puente, P.M.G.; Song, S.; Cao, S.; Rannalter, L.Z.; Pan, Z.; Xiang, X.; Shen, Q.; Chen, F. Garnet-type solid electrolyte: Advances of ionic transport performance and its application in all-solid-state batteries. *J. Adv. Ceram.* **2021**, *10*, 933–972. [CrossRef]
19. Farrukh, M.A.; Butt, K.M.; Chong, K.K.; Chang, W.S. Photoluminescence emission behavior on the reduced band gap of Fe doping in CeO<sub>2</sub>-SiO<sub>2</sub> nanocomposite and photophysical properties. *J. Saudi Chem. Soc.* **2019**, *23*, 561–575. [CrossRef]
20. Del Mar Graciani, M.; Rodríguez, A.; Muñoz, M.; Moyá, M.L. Micellar solutions of sulfobetaine surfactants in water-ethylene glycol mixtures: Surface tension, fluorescence, spectroscopic, conductometric, kinetic studies. *Langmuir* **2005**, *21*, 7161–7169. [CrossRef]
21. Silva, J.M.R.; de Morais Araújo, A.M.; da Costa Evangelista, J.P.; da Silva, D.R.; Gondim, A.D.; de Araujo, A.S. Evaluation of the kinetic and thermodynamic parameters in catalytic pyrolysis process of sunflower oil using Al-MCM-41 and zeolite H-ZSM-5. *Fuel* **2023**, *333*, 126225. [CrossRef]
22. Bhardwaj, G.; Kumar, M.; Mishra, P.K.; Upadhyay, S.N. Kinetic analysis of the slow pyrolysis of paper wastes. *Biomass Convers. Biorefinery* **2023**, *13*, 3087–3100. [CrossRef]
23. Zakariyaou, S.Y.; Ye, H.; Oumarou, A.D.M.; Aziz, M.S.A.; Ke, S. Characterization of Equilibrium Catalysts from the Fluid Catalytic Cracking Process of Atmospheric Residue. *Catalysts* **2023**, *13*, 1483. [CrossRef]
24. Keffer, C.; Mighell, A.; Mauer, F.; Swanson, H.; Block, S. The Crystal Structure of Twinned Low-Temperature Lithium Phosphate. *Inorg. Chem.* **1967**, *6*, 119–125. [CrossRef]
25. Lander, L.; Reynaud, M.; Carrasco, J.; Katcho, N.A.; Bellin, C.; Polian, A.; Baptiste, B.; Rousse, G.; Tarascon, J.M. Unveiling the electrochemical mechanisms of Li<sub>2</sub>Fe(SO<sub>4</sub>)<sub>2</sub> polymorphs by neutron diffraction and density functional theory calculations. *Phys. Chem. Chem. Phys.* **2016**, *18*, 14509–14519. [CrossRef]
26. Huang, Y.X.; Liu, J.Y.; Mi, J.X.; Zhao, J.T. (Ga<sub>0.71</sub>B<sub>0.29</sub>)PO<sub>4</sub> with a high-cristobalite-type structure refined from powder data. *Acta Crystallogr. Sect. E Struct. Rep. Online* **2010**, *66*, i4. [CrossRef]
27. Carbon | XPS Periodic Table | Thermo Fisher Scientific | Thermo Fisher Scientific—CN. Available online: <https://www.thermofisher.cn/cn/zh/home/materials-science/learning-center/periodic-table/non-metal/carbon.html> (accessed on 18 November 2024).

28. Carbon Spectra—Li<sub>2</sub>CO<sub>3</sub>—Lithium Carbonate. Available online: <https://xpsdatabase.net/carbon-spectra-li2co3-lithium-carbonate/> (accessed on 18 November 2024).
29. Al-Kadhi, N.S.; Hefnawy, M.A.; Alamro, F.S.; Pashameah, R.A.; Ahmed, H.A.; Medany, S.S. Polyaniline-Supported Nickel Oxide Flower for Efficient Nitrite Electrochemical Detection in Water. *Polymers* **2023**, *15*, 1804. [CrossRef]
30. Alamro, F.S.; Medany, S.S.; Al-Kadhi, N.S.; Ahmed, H.A.; Hefnawy, M.A. Modified NiFe<sub>2</sub>O<sub>4</sub>-Supported Graphene Oxide for Effective Urea Electrochemical Oxidation and Water Splitting Applications. *Molecules* **2024**, *29*, 1215. [CrossRef]
31. Shulga, Y.M.; Baskakov, S.A.; Knerelman, E.I.; Davidova, G.I.; Badamshina, E.R.; Shulga, N.Y.; Skryleva, E.A.; Agapov, A.L.; Voylov, D.N.; Sokolov, A.P.; et al. Carbon nanomaterial produced by microwave exfoliation of graphite oxide: New insights. *RSC Adv.* **2014**, *4*, 587–592. [CrossRef]
32. Lu, Y.C.; Crumlin, E.J.; Veith, G.M.; Harding, J.R.; Mutoro, E.; Baggetto, L.; Dudney, N.J.; Liu, Z.; Shao-Horn, Y. In Situ Ambient Pressure X-ray Photoelectron Spectroscopy Studies of Lithium-Oxygen Redox Reactions. *Sci. Rep.* **2012**, *2*, 715. [CrossRef]
33. Yin, X.; Sun, X.; Li, D.; Xie, W.; Mao, Y.; Liu, Z.; Liu, Z. 2D/2D Phosphorus-Doped g-C<sub>3</sub>N<sub>4</sub>/Bi<sub>2</sub>WO<sub>6</sub> Direct Z-Scheme Heterojunction Photocatalytic System for Tetracycline Hydrochloride (TC-HCl) Degradation. *Int. J. Environ. Res. Public. Health* **2022**, *19*, 14935. [CrossRef]
34. Liu, X.; Yu, M.; Wu, S.; Gong, J. Composite nanoarchitectonics for efficient lithium storage by encapsulating black phosphorus quantum dots in cobalt/iron based Prussian blue analogues. *J. Alloys Compd.* **2023**, *969*, 172291. [CrossRef]
35. Chatterjee, T.; Raul, C.K.; Mandal, S.; Pradhan, S.K.; Meikap, A.K. Effect of surfactant-assisted hierarchical growth of cupric oxide-hydroxyapatite nanocomposite on the dielectric and electrical transport behavior. *Phys. B Condens. Matter* **2023**, *650*, 414560. [CrossRef]
36. Jung, W.D.; Jeon, M.; Shin, S.S.; Kim, J.S.; Jung, H.G.; Kim, B.K.; Lee, J.H.; Chung, Y.C.; Kim, H. Functionalized Sulfide Solid Electrolyte with Air-Stable and Chemical-Resistant Oxsulfide Nanolayer for All-Solid-State Batteries. *ACS Omega* **2020**, *5*, 26015–26022. [CrossRef]
37. Chen, K.; Tang, Y.; Zhang, S.; Hao, X.; Zhao, X.; Cheng, L.Q.; Xiao, Y.; Wen, Z. Promoted Stability and Reaction Kinetics in Ni-Rich Cathodes via Mechanical Fusing Multifunctional LiZr<sub>2</sub>(PO<sub>4</sub>)<sub>3</sub> Nanocrystals for High Mass Loading All-Solid-State Lithium Batteries. *ACS Appl. Mater. Interfaces* **2024**, *16*, 45459–45472. [CrossRef]
38. Fontecha, D.; Nuwayhid, R.B.; Kozen, A.C.; Stewart, D.M.; Rubloff, G.W.; Gregorczyk, K.E. Low temperature plasma-enhanced atomic layer deposition of sodium phosphorus oxynitride with tunable nitrogen content. *J. Vac. Sci. Technol. A* **2022**, *40*, 032403. [CrossRef]
39. López, E.O.; Bernardo, P.L.; Checca, N.R.; Rossi, A.L.; Mello, A.; Ellis, D.E.; Rossi, A.M.; Terra, J. Hydroxyapatite and lead-substituted hydroxyapatite near-surface structures: Novel modelling of photoemission lines from X-ray photoelectron spectra. *Appl. Surf. Sci.* **2022**, *571*, 151310. [CrossRef]
40. Wang, Y.; Zheng, X.; Qu, Q.; Liu, G.; Battglia, V.S.; Zheng, H. A novel maleic acid/graphite composite anode for lithium ion batteries with high energy and power density. *Carbon* **2018**, *132*, 420–429. [CrossRef]
41. Oxygen | Thermo Fisher Scientific XPS Periodic Table | Thermo Fisher Scientific | Thermo Fisher Scientific—CN. Available online: <https://www.thermofisher.cn/cn/zh/home/materials-science/learning-center/periodic-table/non-metal/oxygen.html> (accessed on 18 November 2024).
42. Khan, Z.; Park, S.O.; Yang, J.; Park, S.; Shanker, R.; Song, H.K.; Kim, Y.; Kwak, S.K.; Ko, H. Binary N,S-doped carbon nanospheres from bio-inspired artificial melanosomes: A route to efficient air electrodes for seawater batteries. *J. Mater. Chem. A Mater.* **2018**, *6*, 24459–24467. [CrossRef]
43. García-Bordejé, E.; Dongil, A.B.; Conesa, J.M.; Guerrero-Ruiz, A.; Rodríguez-Ramos, I. Dual functional materials based on Ni and different alkaline metals on alumina for the cyclic stepwise CO<sub>2</sub> capture and methanation. *Chem. Eng. J.* **2023**, *472*, 144953. [CrossRef]
44. Fang, R.; Li, Y.; Wu, N.; Xu, B.; Liu, Y.; Manthiram, A.; Goodenough, J.B. Ultra-Thin Single-Particle-Layer Sodium Beta-Alumina-Based Composite Polymer Electrolyte Membrane for Sodium-Metal Batteries. *Adv. Funct. Mater.* **2022**, *33*, 2211229. [CrossRef]
45. Foucaud, Y.; Badawi, M.; Filippov, L.O.; Barres, O.; Filippova, I.V.; Lebègue, S. Synergistic adsorptions of Na<sub>2</sub>CO<sub>3</sub> and Na<sub>2</sub>SiO<sub>3</sub> on calcium minerals revealed by spectroscopic and ab initio molecular dynamics studies. *Chem. Sci.* **2019**, *10*, 9928–9940. [CrossRef] [PubMed]
46. Savinova, E.R.; Zemlyanov, D.Y.; Scheybal, A.; Schlögl, R.; Doblhofer, K. Ex Situ X-ray Photoelectron Spectroscopy Study of the Interface between a Ag(111) Electrode and an Alkaline Electrolyte. 2. Structure of the Double Layer. *Langmuir* **1999**, *15*, 6552–6556. [CrossRef]
47. He, X.; Zhu, Y.; Mo, Y. Origin of fast ion diffusion in super-ionic conductors. *Nat. Commun.* **2017**, *8*, 15893. [CrossRef] [PubMed]
48. Du, Y.A.; Holzwarth, N.A.W. Li Ion Diffusion Mechanisms in the Crystalline Electrolyte γ-Li<sub>3</sub>PO<sub>4</sub>. *J. Electrochem. Soc.* **2007**, *154*, A999–A1004. [CrossRef]

**Disclaimer/Publisher's Note:** The statements, opinions and data contained in all publications are solely those of the individual author(s) and contributor(s) and not of MDPI and/or the editor(s). MDPI and/or the editor(s) disclaim responsibility for any injury to people or property resulting from any ideas, methods, instructions or products referred to in the content.